CHIN. PHYS. LETT. Vol. 38, No. 4 (2021) 047501

Spin-Wave Dynamics in an Artificial Kagome Spin Ice

Qiuyang Li(李求洋)[1], Suqin Xiong(熊素琴)[1], Lina Chen(陈丽娜)[2*], Kaiyuan Zhou(周凯元)[3], Rongxin Xiang(项荣欣)[3], Haotian Li(李浩天)[3], Zhenyu Gao(高振宇)[3], Ronghua Liu(刘荣华)[3*], and Youwei Du(都有为)[3]

[1]*China Electric Power Research Institute, Beijing 100192, China*
[2]*School of Science, Nanjing University of Posts and Telecommunications, Nanjing 210023, China*
[3]*School of Physics, Nanjing University, Nanjing 210093, China*

(Received 23 November 2020; accepted 1 February 2021; published online 6 April 2021)

Artificial spin ice (ASI) structures have significant technological potential as reconfigurable metamaterials and magnetic storage media. We investigate the field/frequency-dependent magnetic dynamics of a kagome ASI made of 25-nm-thick permalloy nanomagnet elements, combining magnetoresistance (MR) and microscale ferromagnetic resonance (FMR) techniques. Our FMR spectra show a broadband absorption spectrum from 0.2 GHz to 3 GHz at H below 0.3 kOe, where the magnetic configuration of the kagome ASI is in the multidomain state, because the external magnetic field is below the obtained coercive field $H_c \sim 0.3$ kOe, based on both the low-field range MR loops and simulations, suggesting that the low-field magnetization dynamics of kagome ASI is dominated by a multimode resonance regime. However, the FMR spectra exhibit five distinctive resonance modes at the high-field quasi-uniform magnetization state. Furthermore, our micromagnetic simulations provide additional spatial resolution of these resonance modes, identifying the presence of two high-frequency primary modes, localized in the horizontal and vertical bars of the ASI, respectively; three other low-frequency modes are mutually exclusive and separately pinned at the corners of the kagome ASI by an edge-induced dipolar field. Our results suggest that an ASI structural design can be adopted as an efficient approach for the development of low-power filters and magnonic devices.

DOI: 10.1088/0256-307X/38/4/047501

In the geometrically frustrated system, it is impossible to satisfy the minimum energy constraint of every spin simultaneously. Therefore, geometrical frustration gives rise to a degenerate manifold of ground states, rather than a single stable ground-state configuration, resulting in magnetic analogs of liquids and ice.[1−3] Artificially creating geometrical frustration in the nanomagnetic system, such as artificial spin ice, has become a new and exciting research topic in recent years,[4] with potential for use in applications such as reconfigurable metamaterials for tailoring spin-wave properties, and magnonic devices for information transmission and storage.[5−6] The spin arrangement of spin ice, analogous to the spatial structure between hydrogen and oxygen in ice, has two spins pointing into, and two pointing away from the center.[2] Therefore, this spin arrangement rule is called the "ice rule". Since artificial spin ices can be used to investigate the collective behavior of magnetically interacting systems for understanding their complex dynamics, numerous ASI lattices have been theoretically proposed and experimentally studied, e.g., square spin ice,[1,3,7−11] kagome spin ice,[12,13] the shakti lattice,[14] the Cairo lattice,[15] and the quadrupole lattice.[16] However, the majority of studies have focused on thermalization processes and slow dynamics, such as ground state, thermal relaxation, and magnetic reversal processes,[7−16] and very few works in the past few years have examined collective magnetization dynamics in the GHz microwave regime.[17−20]

In this work, we investigate the magnetic dynamics of a kagome ASI of $Ni_{80}Fe_{20}$ (Py) by combining nano-patterned coplanar waveguide (CPW) and broadband ferromagnetic resonance techniques. The magnetization reversal processes beyond the single-domain situation at low fields, and several distinct dynamical modes of kagome ASI structures at high fields are investigated in detail via magnetotransport and differential FMR, respectively. Firstly, we determine the shape anisotropy field and the magnetic field range corresponding to the multidomain or multivortex dominated regime in terms of magnetoresistance hysteresis hoops and low-field anisotropy magnetoresistance (AMR). The FMR spectra show that ASI exhibits a broadband absorption spectrum, from 0.2 GHz to ∼3 GHz at the field below 0.3 kOe, associated with the five distinct multidomain structure res-

Supported by the State Grid Corporation of China via the Science and Technology Project: Research on Electromagnetic Measurement Technology Based on EIT and TMR (Grant No. JL71-18-007).
*Corresponding authors. Email: chenlina@njupt.edu.cn; rhliu@nju.edu.cn
© 2021 Chinese Physical Society and IOP Publishing Ltd

onance peaks observed at high fields, are related to different spin-wave modes. Finally, a micromagnetic simulation quantitatively reproduces our experimental observations of static and dynamic magnetic behavior, and provides more detailed spatial profiles of the spin-wave modes.

Figure 1 shows a schematic of the experimental setup and kagome ASI sample structure. The 2D kagome ASI structure is patterned over an area of $70 \times 25\,\mu\text{m}^2$ on the S-pole of a CPW, composed of a 50-nm thick gold layer, via a combination of electron-beam lithography and magnetron sputtering. The 2D kagome ASI sample is constructed using 25-nm-thick Py in a hexagonal honeycomb pattern. The length and width of one magnetic pole are 1000 nm and 250 nm, respectively. Figure 1(b) shows their scanning electron microscope (SEM) images. All transport and differential FMR spectra measurements were carried out at room temperature. For the magnetoresistance measurements, a 5 mA dc current was applied at the 50-nm-thick gold S-pole, and the magnetic field was oriented at an in-plane angle θ relative to the current flow (or the gold S-pole). In order to achieve a good signal-to-noise FMR signal, an ac Oersted field, perpendicular to the static bias magnetic field at an orientation angle of $\theta = 0$, was generated through the S-pole via connecting the CPW with a microwave generator. Meanwhile, the bias magnetic field was further modulated by means of a pair of secondary Helmholtz coils, powered by an alternating current source at 500 Hz [Fig. 1(a)].[21]

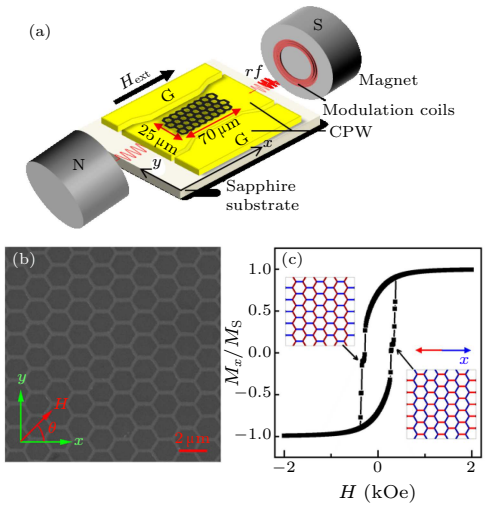

Fig. 1. (a) MR and differential FMR spectra experimental setup. (b) SEM image of the kagome ASI structure ($70 \times 25\,\mu\text{m}^2$), comprising 25-nm-thick Py hexagonal wire netting (length = 1000 nm and width = 250 nm). (c) Magnetic hysteresis loop of the numerical simulation at $\theta = 0$. Inset: snapshot of the magnetization configuration of ASI obtained via micromagnetic simulation near the coercive field $\pm H_c$, indicated by the straight arrows. The blue and red colors represent the magnetization component m_x, parallel and antiparallel to the x-axis, respectively.

In addition, micromagnetic simulations of the ASI structure were performed [Fig. 1(b)] using the MuMax3 package.[22] The parameters used in the simulations are as follows: exchange constant $A = 1.3 \times 10^{-11}\,\text{J/m}^3$, saturation magnetization $M_S = 5.3 \times 10^5\,\text{A/m}$, damping coefficient $\alpha = 0.01$, for a cell size measuring 10 nm × 10 nm × 25 nm. Figure 1(c) shows the magnetic hysteresis loop obtained via simulation in the field range of ±2 kOe. Two platforms of the normalized magnetization component $m_x = 0$, near to and below the coercive field $\pm H_c \sim 0.27$ kOe, indicate that the magnetization $\boldsymbol{M}$ of the nanomagnet elements is oriented along the long side, due to the shape anisotropy field H_a. The inset of Fig. 1(c) illustrates the magnetization $\boldsymbol{M}$ orientation of the kagome ASI.

To experimentally obtain the magnetic properties of the microscale ASI sample, we performed various magnetoresistance measurements by changing the amplitude and the orientation of the magnetic field relative to the current flow. Figures 2(a)–2(d) show the magnetic field-dependent MR curves of ASI grown on a 50-nm-thick Au layer at four selected in-plane field angles. For all magnetic field angles, MR exhibits two sudden transitions near ±0.25 kOe, due to the shape anisotropy field H_a, since the coercivity of the Py film did not exceed 2–3 Oe,[23] suggesting that the magnetization of ASI undergoes a sudden reversal, forming a multidomain or multi-vortex state below $\pm H_c \sim 0.3$ kOe, closing to the calculated value ∼0.27 kOe in the above simulation. To quantitatively determine the shape anisotropy field H_a, we further performed the angular dependence of MR with several low fields. The well-defined sinusoidal dependence of resistance R on the orientation of H with a period of 180, measured using a high $H = 0.6$ kOe, was consistent with the anisotropic magnetoresistance of Py, suggesting that the equilibrium orientation of M was parallel to the magnetic field at $H > 0.6$ kOe. The relative magnetoresistance was $\Delta R/R = [R(0) - R(90°)]/R(90°) = 0.27\%$, much smaller than in stand-alone Py films, due to shunting by the bottom Au layer. However, the AMR curves, obtained at low fields of $H < 0.4$ kOe, significantly diverged from the sinusoidal function, indicating that the direction of $\boldsymbol{M}$ is no longer aligned with the applied magnetic field H. The AMR of the Py film can be described by $R(\beta) = R_0 + \frac{\Delta R}{2}\cos(2\beta)$, where β is the angle between the magnetization M and the current direction.[24] The free energy can be expressed as $\varepsilon = \frac{1}{2}\mu_0 M_S H_K \sin^2\beta - \mu_0 \boldsymbol{H}\cdot\boldsymbol{M}_S$, where $H_K = 4\pi N M$ is the effective anisotropy field caused by the anisotropic shape of the magnetic element, where N is the demagnetization factor. The equilibrium orientation of magnetization can be determined by minimizing the free energy to β, yielding $\sin(\theta -$

$\beta) = \frac{H_K}{2H}\sin(2\beta)$, a well-known result of the Stoner–Wohlfarth model. Considering the symmetry of the Py kagome lattice, we can divide the ASI array into a 120° Y-shaped pole to analyze the total AMR, using the integral formula $R = R_0 + \sum_{i=1,2,3} \Delta R_i \cos^2(\beta_i)$. Fitting the low-field AMR curves obtained at 0.2 kOe and 0.4 kOe [see Figs. 2(f) and 2(g)], we can quantitatively extract $H_a \sim H_K = 0.3$ kOe. Therefore, the kagome ASI has a significantly larger coercive field H_c than that of the uniform Py film, due to a nanostructure-induced larger shape anisotropy H_a.

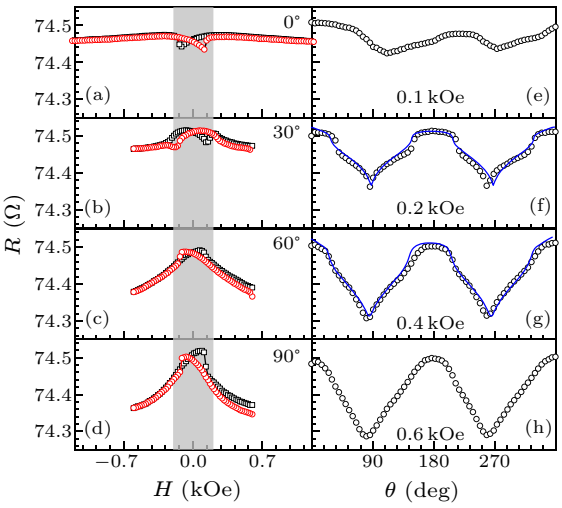

Fig. 2. (a)–(d) Magnetoresistance hysteresis loops of a 25-nm-thick Py-ASI structure on top of a 50-nm-thick Au layer at the selected external magnetic field angle $\theta = 0$ (a), 30° (b), 60° (c), and 90° (d). The multidomain or multi-vortex regime after sudden magnetization reversal at low fields is indicated by the shaded area. (e)–(i) AMR curves of this ASI-Au at $H = 0.1$ kOe (e), 0.2 kOe (f), 0.4 kOe (g), and 0.6 kOe (h). The solid lines in (f) and (g) are the results of fitting with the AMR formula and the Stoner–Wohlfarth model discussed in the text.

Our central experimental result involves the magnetic-field- and frequency-dependent magnetodynamics of the kagome ASI structure. To explore ASI dynamics in greater detail, we established the broadband FMR absorption spectra using differential FMR techniques with both field and frequency sweep modes.

Figure 3 shows the experimental FMR spectra of the kagome ASI obtained by sweeping the excitation rf signal from 0.1 GHz to 10 GHz in the field range of ±1 kOe along the x-axis ($\theta = 0$). Five distinct narrow resonance peaks are observed in the pseudocolor maps of the field-dependent FMR spectra, as marked by the dashed lines in Fig. 3. Moreover, the FMR spectra show a broad absorption band from 0.2 GHz to ∼3 GHz at the low-field range of ±0.3 kOe, associated with the multidomain or multi-vortex regime confirmed by the magnetoresistance hysteresis loops shown in Figs. 2(a)–2(d). The frequency vs field dispersion curves of spin-wave modes, marked as dashed lines, are identical for positive and negative fields, and are symmetrical around the zero field, due to the structural symmetry of the kagome ASI. The FMR signal amplitude primarily depends on the actual rf current, determined by the loss of the rf microwave measuring circuit, and the output power of the microwave generator. The input loss of an rf microwave circuit always depends on its frequency. Therefore, FMR spectra obtained via the sweeping frequency of the rf signal have a low signal-to-noise ratio.

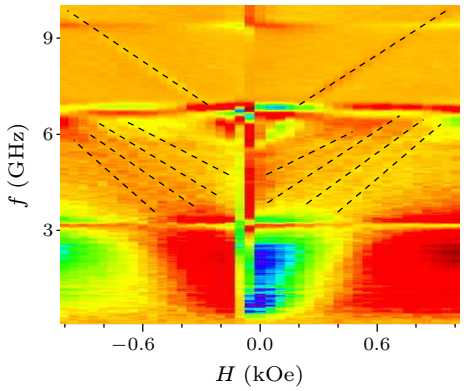

Fig. 3. Pseudocolor map of the experimental FMR spectra of ASI, obtained using a sweeping rf signal from 0.2 GHz to 10 GHz with the in-plane magnetic field along the x-axis ($\theta = 0$). The dashed lines are guides to the eyes.

To achieve high sensitivity and an enhanced FMR signal, we adopt the differential FMR method, with a voice frequency-modulated bias magnetic field, sweeping from $H = 1.3$ kOe to zero at a constant frequency f. The modulation amplitude and frequency of the magnetic field are about 3 Oe and 500 Hz, respectively. Figure 4(a) shows a pseudocolor map of the derivative of the absorbed power (dP/dH) with H sweep mode detected by a lock-in. Based on the pseudocolor map of dP/dH, one can clearly see five curves of frequency vs field dispersion, consistent with the observed results in Fig. 3. The highest frequency mode exhibits the maximal spectral intensity, because this mode occupies the total horizontal portion of the kagome ASI, and has the optimal FMR excitation condition, as verified in the following discussion. Unlike the frequency sweep, however, the broad absorption band from 0.2 GHz to ∼3 GHz at $H < 0.3$ kOe is inaccessible to the field sweep, as the multidomain or multi-vortex becomes unstable during the scanning field process.

To obtain a greater insight into the experimentally observed spin-wave modes, we perform micromagnetic simulations using Mumax3 for this kagome ASI structure, based on a 15 μm × 15 μm square, divided into $50 \times 50 \times 25$ nm^3 cells. Figure 4(b) shows the pseudocolor plots of the intense power of FMR spectra obtained via micromagnetic simulations at in-plane magnetic field H, varied between 0 and 1.2 kOe in 0.05 kOe steps with the orientation along the x-axis. The frequency vs field dispersion is in reasonable agreement

with the experimental observations discussed above in Figs. 3 and 4(a). Furthermore, the higher FMR modes have a greater spectral intensity, consistent with the experimental observations in Fig. 4(a).

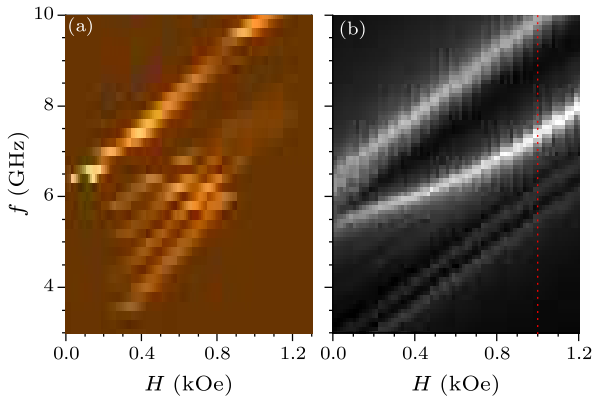

Fig. 4. Experimental (a) and simulated (b) FMR spectra for the ASI system at $\theta = 0$. The experimental FMR spectra were obtained by sweeping field H from 1.3 kOe to 0.

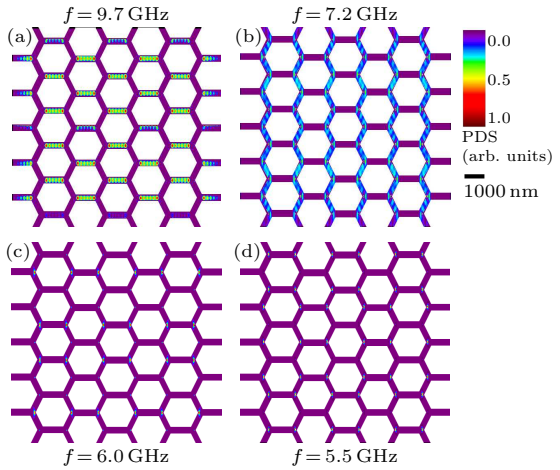

Fig. 5. Simulated mode profiles of spin-wave modes with the labeled resonance frequencies $f = 9.7$ GHz (a), $f = 7.2$ GHz (b), $f = 6.0$ GHz (c), and $f = 5.5$ GHz (d), at applied magnetic field $H = 1$ kOe. Color scale indicates the power amplitude of the modes.

To gain further insight into the spatial profile of these dynamical modes, excited in the kagome ASI structure, we also calculate normalized spatial power maps of the four observed dynamical modes, where $f = 9.7$ GHz, 7.2 GHz, 6 GHz, and 5.5 GHz at $H = 1.0$ kOe, obtained from the time dependence of the local magnetization component m_x^2 (Fig. 5), by performing pointwise temporal FFT over the simulated area. Figures 5(a) and 5(b) show that the dynamical modes where $f = 9.7$ GHz and 7.2 GHz at $H_{\rm ext} = 1.0$ kOe, i.e., those with the highest intensity in the FMR spectra of Fig. 4(b), are localized in the horizontal and the vertical nanowires, respectively. Based on the periodic intensity distribution along their long side, they can be identified as standing backward volume magnetostatic spin-waves (BVMSWs), pinned by the edges due to the geometric demagnetization effect.[25] Based on the quantum confinement effect, the wave vectors, k, of two primary quantized standing BVMSWs can also be estimated from the node numbers n of the standing spin-waves, using the formula $k = n\pi/L$, where L is the confinement length of the magnetic nanobars. The standing BVMSW mode localized in the horizontal nano-bars has a wave vector $k \sim 0.188\,\mathrm{nm}^{-1}$, while k is $0.126\,\mathrm{nm}^{-1}$ for the mode localized in the vertical nanobars. The low-frequency modes with a lower power intensity than that of the two primary horizontal and vertical modes are localized separately in the corners of the hexagonal kagome lattice by the edge-induced stray field, due to dipolar interaction at the corners, as shown in Figs. 5(c) and 5(d), respectively. It should be noted that these edge modes exhibit spatial-periodic structure and mutual exclusive distribution in the corners of the kagome lattice, relative to the periodic boundary conditions of the kagome lattice.[26]

In summary, we have experimentally characterized the static and dynamical properties of 25-nm-thick Py kagome ASI lattices in 70 μm×25 μm rectangle area by combining magnetoresistance hysteresis loop, AMR, and microscale CPW-FMR techniques. The MR hysteresis loops reveal that the kagome ASI is in a multidomain or multi-vortex state below $\pm H_{\rm c} \sim 0.3$ kOe due to the shape anisotropy field, edge-induced dipolar field, and magnetic frustration effect of geometry-induced spin-ice structures. Moreover, we also determine the quantitative value of the shape anisotropy field $H_{\rm a} \sim 0.3$ kOe, from the AMR curves at the low fields $H = 0.2$ kOe and 0.4 kOe. Furthermore, frequency-dependent FMR spectra with a very broad peak at $H < 0.3$ kOe, obtained via frequency sweeping mode at the constant fields, suggest that the multimode resonances dominate the magnetodynamics of ASI, further confirming the low-field multidomain or multi-vortex structure observed in the MR experiments stated above. However, at the high-field range, the FMR spectra exhibit five distinctive resonance peaks, corresponding to five distinct spin-wave modes. Our simulations provide an additional spatial profile for these modes, revealing that two primary modes with a high-frequency are localized in the horizontal and vertical legs of the ASI, respectively. In comparison, two other modes with lower spectral intensity are mutually exclusive, and separately pinned at the corners of the ASI by the edge-induced dipolar field. Our results suggest that the kagome ASI structure could be used for microwave filters and spin-wave-based devices.[27,28]

References

[1] Wang R F, Nisoli C, Freitas R S, Li J, McConville W, Cooley B J, Lund M S, Samarth N, Leighton C, Crespi V H and Schiffe P 2006 *Nature* **439** 303

[2] Castelnovo C, Moessner R and Sondhi S L 2008 *Nature* **451** 42

[3] Morgan J P, Stein A, Langridge S and Marrows C H 2011 *Nat. Phys.* **7** 75

[4] Nisoli C, Moessner R and Schiffer P 2013 *Rev. Mod. Phys.* **85** 1473

[5] Skjaervo S H, Marrows C H, Stamps R L and Heyderman L J 2020 *Nat. Rev. Phys.* **2** 13

[6] Gliga S, Iacocca E and Heinonen O G 2020 *APL Mater.* **8** 040911

[7] Farhan A, Derlet P M, Kleibert A, Balan A, Chopdekar R V, Wyss M, Perron J, Scholl A, Nolting F and Heyderman L J 2013 *Phys. Rev. Lett.* **111** 057204

[8] Gliga S, Hrkac G, Donnelly C, Buchi J, Kleibert A, Cui J, Farhan A, Kirk E, Chopdekar R V, Masaki Y, Bingham N S, Scholl A, Stamps R L and Heyderman L J 2017 *Nat. Mater.* **16** 1106

[9] Wang Y L, Xiao Z L, Snezhko A, Xu J, Ocola L E, Divan R J, Pearson E, Crabtree G W and Kwok W K 2016 *Science* **352** 962

[10] Nisoli C, Kapaklis V and Schiffer P 2017 *Nat. Phys.* **13** 200

[11] Xie Y L, Du Z Z, Yan Z B and Liu J M 2015 *Sci. Rep.* **5** 15875

[12] Canals B, Chioar I A, Nguyen V D, Hehn M, Lacour D, Montaigne F, Locatelli A, Mentes T O, Burgos B S and Rougemaille N 2016 *Nat. Commun.* **7** 11446

[13] Zhao K, Deng H, Chen H, Ross K A, Petříček V, Günther G, Russina M, Hutanu V and Gegenwart P 2020 *Science* **367** 1218

[14] Gilbert I, Chern G W, Zhang S, O'Brien S L, Fore B, Nisoli C and Schiffer P 2014 *Nat. Phys.* **10** 670

[15] Saccone M, Hofhuis K, Huang Y L, Dhuey S, Chen Z, Scholl A, Chopdekar R V, van Dijken S and Farhan A 2019 *Phys. Rev. Mater.* **3** 104402

[16] Sklenar J, Lao Y, Albrecht A, Watts J D, Nisoli C, Chern G W and Schiffer P 2019 *Nat. Phys.* **15** 191

[17] Zhou X, Chua G L, Singh N and Adeyeye A O 2016 *Adv. Funct. Mater.* **26** 1437

[18] Bhat V S, Heimbach F, Stasinopoulos I and Grundler D 2017 *Phys. Rev. B* **96** 014426

[19] Talapatra A, Singh N and Adeyeye A O 2020 *Phys. Rev. Appl.* **13** 014034

[20] Bhat V S, Watanabe S, Baumgaertl K, Kleibert A, Schoen M A W, Vaz C A F and Grundler D 2020 *Phys. Rev. Lett.* **125** 117208

[21] Fu Q W, Li Y, Chen L N, Ma F S, Li H T, Xu Y B, Liu B, Liu R H and Du Y W 2020 *Chin. Phys. Lett.* **37** 087503

[22] Vansteenkiste A, Leliaert J, Dvornik M, Helsen M, Garcia-Sanchez F, Van Waeyenberge B 2014 *AIP Adv.* **4** 107133

[23] Liu R H, Lim W L and Urazhdin S 2013 *Phys. Rev. Lett.* **110** 147601

[24] Eijkel K J 1988 *IEEE Trans. Magn.* **24** 1957

[25] Bailleul M, Holinger R and Fermon C 2006 *Phys. Rev. B* **73** 104424

[26] Zhang G F, Li Z X, Wang X G, Nie Y Z and Guo G H 2015 *Chin. Phys. B* **24** 097503

[27] Kruglyak V V, Demokritov S O and Grundler D 2010 *J. Phys. D* **43** 264001

[28] Li L Y, Chen L N, Liu R H and Du Y W 2020 *Chin. Phys. B* **29** 117102